

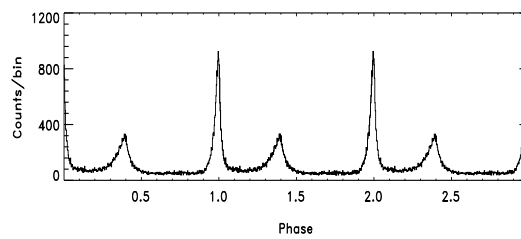
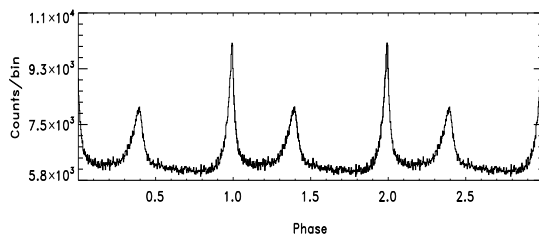
---

BACHELOR THESIS

---

The “absolute” timing behaviour of the Crab pulsar at X-rays and gamma-rays

---



---

*Author:*  
Dirk SCHOLTE  
*Study:*  
Physics & Astronomy  
Utrecht University

*Supervisor:*  
Dr. Lucien KUIPER  
SRON  
*Utrecht University contact:*  
Dr. Enrico PAJER  
Utrecht University

January 18, 2017



## Abstract

In this bachelor thesis I have updated the high-energy “absolute” timing picture of the Crab pulsar by including the Fermi LAT gamma-ray data ( $>100$  MeV) collected from the start of the Fermi science operations (4-8-2008) until October 2016, and the XMM-Newton EPIC PN data by analysing the bi-yearly Crab timing observations taken in Burst and Timing mode (0.3-12 keV). This bachelor thesis also uses the high-energy “absolute” timing measurements of INTEGRAL IBIS ISGRI (20-300 keV, from the INTEGRAL launch date until October 2016) and RXTE PCA (3-32 keV, from the INTEGRAL launch date until its decommissioning at 5-1-2012). The Jodrell Bank Observatory Crab pulsar monthly ephemerides have served as baseline for all these “absolute” timing measurements. These ephemerides have been reliable in almost all months analysed in this study. There were a small number of cases in which suspected behaviour (outliers) has been discovered. Excluding outliers, the average time shift between the gamma-ray pulse maximum and the radio pulse maximum for Fermi LAT is  $-111\pm 4$   $\mu\text{s}$ . For XMM Newton I found, again excluding outliers, for the EPIC PN operating in Burst mode a time shift  $-353\pm 4$   $\mu\text{s}$  and  $-271\pm 4$   $\mu\text{s}$ , when EPIC PN operates in Timing mode. This apparent discrepancy means that Burst and Timing mode data should not be mixed. INTEGRAL IBIS ISGRI data, excluding outliers, showed a time shift of  $-248\pm 2$   $\mu\text{s}$ , consistent with an earlier measurement (Kuiper et al. (2003)) correcting for an additional ground station delay of 47  $\mu\text{s}$ . Finally, for RXTE PCA a value of  $-297\pm 3$   $\mu\text{s}$  has been derived, which is consistent within statistical and systematical margins with previous values, estimated by Rots et al. (2004) and Molkov et al. (2010). Combining the results across the X-ray, hard X-ray, soft gamma-ray and  $>100$  MeV gamma-ray bands no evidence is found for a linear trend in the time delays, as found by Molkov et al. (2010).

**Keywords:** pulsars: individual: PSR B0531+21 — radio, X-rays, and gamma-rays

**Title page images:** Top: Composite image of the Crab pulsar and nebula. Blue indicates X-rays (from Chandra), green is optical (from the HST), and red is radio (from the VLA)[1]. Bottom left: Pulse-phase distribution of the Crab pulsar in X-rays obtained by XMM Newton EPIC PN (0.3-12 keV). Bottom right: Pulse-phase distribution of the Crab pulsar in gamma-rays obtained by Fermi LAT ( $>100$  MeV).



# Contents

<b>1</b>	<b>Introduction</b>	<b>1</b>
1.1	Stellar evolution . . . . .	1
1.2	Neutron stars and pulsars . . . . .	2
1.2.1	The Crab pulsar (PSR B0531+21) . . . . .	3
1.2.2	Pulsar timing . . . . .	4
1.3	Research objectives . . . . .	4
<b>2</b>	<b>Instrumentation</b>	<b>6</b>
2.1	Fermi LAT . . . . .	6
2.2	XMM Newton EPIC PN . . . . .	7
2.3	INTEGRAL IBIS ISGRI . . . . .	8
2.4	RXTE PCA . . . . .	9
<b>3</b>	<b>Data analysis</b>	<b>10</b>
3.1	The Jodrell Bank Observatory monthly Crab pulsar ephemerides . . . . .	10
3.2	Preparation for timing analysis . . . . .	10
3.2.1	XMM Newton EPIC PN raw data processing . . . . .	10
3.2.2	Barycentering . . . . .	11
3.3	Timing analysis . . . . .	11
3.3.1	Phase folding . . . . .	11
3.3.2	Cross-correlation of lightcurves . . . . .	12
3.4	Statistical analysis of distributions . . . . .	13
3.4.1	Skewness and kurtosis . . . . .	13
<b>4</b>	<b>Results</b>	<b>14</b>
4.1	“Absolute” timing distributions . . . . .	18
4.1.1	Fermi LAT . . . . .	18
4.1.2	XMM Newton EPIC PN . . . . .	19
4.1.3	INTEGRAL IBIS ISGRI . . . . .	21
4.1.4	RXTE PCA . . . . .	22
4.2	JBO monthly ephemerides of the Crab pulsar . . . . .	23
4.2.1	Uncertainty in the ephemerides . . . . .	23
4.2.2	Trends of outliers within ephemerides . . . . .	24
4.3	Radio delay evolution with energy . . . . .	27
<b>5</b>	<b>Discussion and conclusions</b>	<b>28</b>
<b>6</b>	<b>Acknowledgement</b>	<b>30</b>



# Chapter 1

## Introduction

In this chapter the basic astrophysical background information important for this bachelor thesis is discussed.

### 1.1 Stellar evolution

The fate of stars at the end of their lifetime is largely determined by the mass of the star. Stars are formed when clouds of gas in the interstellar medium collapse. During this collapse a planetary disk is formed, where a protostar starts to form in the centre. If the mass of the protostar is large enough ( $M > 0.08M_{\odot}$  [2]) Hydrogen fusion will start in the core. This start of Hydrogen fusion signifies the start of a star's main sequence lifetime. Stars spend most of their lifetime as main sequence stars, but when the Hydrogen in their core starts to run out, stars of different masses behave in different ways.

The hydrostatic balance between the thermal pressure caused by nuclear fusion and pressure exerted by gravity is broken when the Hydrogen supply in the core of the star is depleted. Due to this the core collapses and transforms gravitational energy into thermal energy. Depending on the mass of the star the collapse can cause the start of Hydrogen fusion in the shell around the core of the star. The Helium produced in this process adds to the pressure on the core. This pressure keeps increasing until the Hydrogen in the shell is depleted or electron degenerate pressure is reached. The Pauli exclusion principle states that any two identical fermions can not occupy the same quantum state, this results in a minimum pressure at which fermions do not occupy the same state. For electrons this pressure is the electron degeneracy pressure.

At this constant pressure the mass of the core keeps growing as nuclear fusion takes place. This results in an increased temperature of the core of the star. For stars of a mass  $M > 0.5M_{\odot}$  [2] the nuclear fusion of higher elements will take place, whereas in lighter stars the nuclear fusion will stop when the Hydrogen in the shell around the core is depleted. The continuing fusion leads to an increasingly heavy core. The electron degenerate pressure that supports the core has a limit to the mass under which it can be sustained. When the mass of the core of the star reaches about  $M > 1.4M_{\odot}$  [2], the Chandrasekhar limit, the electron degenerate pressure can no longer be sustained. In most stars the core will never reach this critical mass. In these stars nuclear fusion stops before the core reaches this critical mass. The remnants of these stars are called white dwarfs, stellar remnants composed mostly of electron degenerate matter.

There are stars, however, for which fusion continues up to the point where the core of the star reaches a mass of about 1.4 Solar masses. A core this massive is no longer

supported by electron degenerate pressure. At this point electrons and protons combine and form neutrons and electron neutrinos. This process results in a further collapse of the core of the star. This collapse stops when degenerate pressure is reached again, not electron degenerate pressure this time but neutron degenerate pressure. Neutrons are fermions just like electrons and therefore obey the Pauli exclusion principle. This collapse of the core of a heavy star is accompanied by an explosion called a supernova. There are two kinds of stellar remnants that can be left behind by a supernova, a black hole or a neutron star. The latter of these will be discussed in the next section.

A Black hole is an object of which the escape velocity is larger than the speed of light. The radius at which an object has an escape velocity equal to the speed of light is called the Schwarzschild radius. For an object to be a black hole it needs to be squeezed until it has a radius smaller than the Schwarzschild radius. Only the most heavy stars have enough mass to become a black hole at the end of their lifetime.[2]

## 1.2 Neutron stars and pulsars

The minimal initial mass for a star to become a neutron star is about  $7 - 8M_{\odot}$  [2]. When these stars are at the stage in their life cycle, where their core reaches the mass where it can no longer be sustained by electron degenerate pressure, they go through an event called a supernova. Supernova are explosive events, where the luminosity of the star increases dramatically for a short time. The different kinds of supernova events are called type Ia, Ib, and II. Only type Ib and II can leave a neutron star behind. For these types of supernovae during the collapse of the core, the main energy source is the conversion of gravitational potential energy. This results in significant brightening. During this event the outer layers of the star are blown away as the core collapses into a small volume. These blown away outer layers disperse in the interstellar medium around the supernova remnant and form a nebula. In the middle remains the collapsed core of the star. If the radius of the core is larger than its Schwarzschild radius the remnant is called a neutron star. Neutron stars are stellar remnants made up out of neutron degenerate matter.

In the process of the core collapse of a star, its angular momentum is conserved. This often results in a very high rotational speed of the neutron star. The period of rotation of neutron stars can be on the order of a few milliseconds. During the collapse of the core the magnetic flux through the stellar material is also conserved. This results in strong magnetic fields produced by neutron stars. The rotating magnetic field creates a strong electric field.

When the (radio) beams of the rapidly spinning neutron stars cross the observer's line of sight we speak of pulsars.

The electro-magnetic radiation of a pulsar is mainly produced through 4 processes: cyclotron radiation, synchrotron radiation, curvature radiation, and inverse Compton radiation. Cyclotron and synchrotron radiation are produced when a charged particle is accelerated radially (acceleration transverse to its motion) in a homogeneous magnetic field. Synchrotron radiation is only produced when the particle is gyrating at relativistic speeds. Curvature radiation is produced in the very high magnetic field of the pulsar magnetosphere where an electron or positron is constrained to follow the path of a magnetic field line very closely. The curvature of the field line forces the particle to accelerate transversely to its motion, this causes the particle to radiate. Inverse Compton radiation is caused by the transfer of energy of high-energy electrons to radiation. This

effect can produce very energetic radiation.

There are two main emission regions in the pulsar magnetosphere, the polar slot gap and the outer slot gap. The polar slot gap is the location of radio emission for most pulsars. In both the polar slot gap and outer slot gap radiation is produced mostly through synchrotron and curvature radiation. The emission regions are connected, the location of these regions is shown in Figure 1.1. The radiation from these emission regions is emitted in beams that are aligned with the pulsar's magnetic poles.[4]

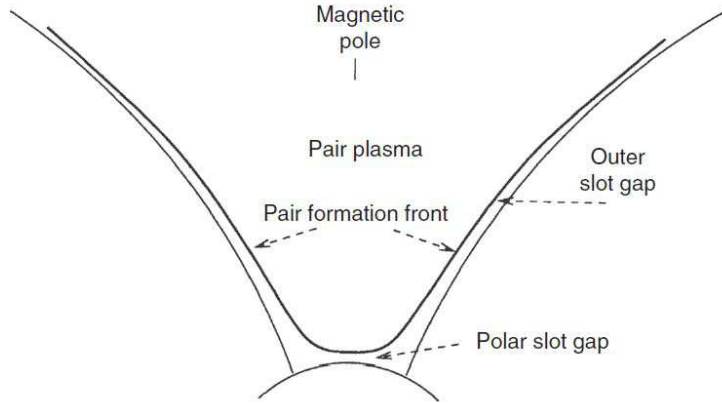


Figure 1.1: Diagram of part of a pulsar magnetosphere. The polar slot gap and outer slot gap are pointed out. These two regions are the main emission regions in the pulsar magnetosphere. Source: [4]

### 1.2.1 The Crab pulsar (PSR B0531+21)

The Crab pulsar or PSR B0531+21 is a 33 ms pulsar ( $\sim 30$  Hz; [3]) located at the centre of the Crab nebula. The Crab pulsar and nebula are the remnants of a supernova observed over 900 years ago [4]. The location of the Crab pulsar in celestial coordinates ( $\alpha_{2000}, \delta_{2000}$ ) is ( $05^h 34^m 31.97232^s, +22^h 00^m 52.0690^s$ ) [19]. Around the 1940's both the star in the centre of the Crab nebula and the nebula itself were documented as the remnants of this supernova. The brightness of the radiation of the nebula was much higher than expected from the remaining energy of the supernova, which indicated a different energy source. In the following decades the Crab nebula was observed by several observatories. This, in combination with technical developments, eventually resulted in the detection of the individual pulses of the central star of the nebula. In 1970 [4] it was shown that there was another energy source for the radiation of the Crab nebula. The central star in the nebula was identified as the Crab pulsar, which provided the energy of the emanating radiation from the nebula.

The Crab pulsar has been monitored by the Jodrell Bank Observatory for almost 50 years and its rotational behaviour is well documented in monthly ephemerides. In general the rotation frequency of the Crab pulsar is remarkably uniform and decreases slowly, except during some events called glitches. These glitches are sudden events where the rotation frequency (and/or its derivatives) abruptly and unexpectedly changes, the Jodrell Bank Observatory had documented 24 of these events up to 2014. [3]

## 1.2.2 Pulsar timing

Pulsar timing observations aim to measure accurately the arrival time of a pulsar radiation beam at an observatory (either Earth bound or spacecraft borne) and relate this to the time of emission at the distant astrophysical source.

In this process we have to determine the pulse arrival in a frame centered on the Solar System barycentre, the best conceivable inertial system to describe dynamical processes. This involves arrival time corrections due to a) geometry (sometimes called Römer delay), b) propagation through interstellar medium (ISM) (dispersion measure (DM) correction, which is proportional to  $\nu_{obs}^{-2}$  with  $\nu_{obs}$  the observing frequency), c) motion in a time dependent potential field of the entire Solar System (gravitational redshift and time delay; Einstein delay), and d) space-time curvature in the Solar System (Shapiro delay; mainly effective for source sky locations in the neighbourhood of the Sun).

For the geometry correction we need an accurate celestial location of the source of interest, a proper description of the orbit of a space-borne instrument with respect to the Earth centre or accurate geographical coordinates of the Earth bound observatory and position of Earth centre with respect to Solar System barycentre. The latter is provided by the JPL Solar System planetary ephemerides (either the DE200, DE405 or DE421 series).

Corrections for the propagation of the radiation through the (patchy) interstellar medium, DM corrections, are only significant for observations at radio frequencies, and these can be completely ignored for observations at X-rays and gamma-rays. At radio frequencies, however, fluctuations in the DM due to variations in the number of free electrons along the line-of-sight (interstellar 'weather') give rise to time-dependent DM corrections (often modelled by a linear model), which further increase the uncertainty in pulse arrival time.

From pulsar timing we can obtain a wealth of astrophysical information [4] on the nature of the source (e.g. from the spin frequency  $\nu$  and slow-down rate  $\dot{\nu}$  we can estimate of the age and magnetic field strength of the pulsar), on its location and (proper) motion through our Galaxy, and on the ionised gas component of the ISM through DM estimates.

In this bachelor thesis the pulse arrival time at X-rays (XMM-Newton and RXTE PCA) and gamma-rays (INTEGRAL ISGRI and Fermi LAT) of the Crab pulsar with respect to radio frequencies (Jodrell Bank Observatory) is derived as a function of time across multi-year baselines adopting the rotation characteristics derived at a monthly base by the Jodrell Bank Observatory. This process is often called “absolute” timing monitoring of the Crab pulsar.

## 1.3 Research objectives

The 33 ms pulsar in the Crab nebula, PSR B0531+21, is an excellent source for timing calibration purposes because this rapidly spinning neutron star is (brightly) detectable across a very broad spectral range from the radio- up to the TeV gamma-ray domain. Regular timing calibration observations are (have been) performed by high-energy instruments aboard various spacecrafts during their mission lifetime e.g. by the RXTE PCA (3-32 keV; 5-1-2012 decommissioned), by INTEGRAL ISGRI (20-300 keV; ongoing), and XMM-Newton EPIC-pn (0.3-12 keV; ongoing). Also, the Large Area Telescope (LAT; >20 MeV) aboard the Fermi spacecraft and the Gamma-ray Burst Monitor

(GBM; 5-2000 keV) continuously have the Crab pulsar in their field of view during the all-sky survey mode, making continuous timing calibration possible.

The Jodrell Bank radio Observatory (UK) maintains an up-to-date database of the timing characteristics (ephemerides) stored on a monthly base. This database is used as a baseline for “absolute” timing calibration of the above mentioned high-energy instruments. Currently, the picture is up-to-date and complete for INTEGRAL ISGRI (still ongoing) and RXTE PCA, while the XMM Newton picture is incomplete with many gaps and the Fermi LAT picture is completely missing.

In this bachelor thesis I will work on expanding the full high-energy picture by including the Fermi LAT high-energy gamma-ray data ( $>100$  MeV) collected since the Fermi launch until October 2016 and will fill in the gaps for the XMM-Newton EPIC pn by analysing the bi-yearly Crab timing observations taken in Burst and Timing mode.

A stable behaviour of the internal clocks/oscillators aboard the above mentioned high-energy instruments is of utmost importance in studying fast timing phenomena of astrophysical objects and thus a continuous monitoring of the “absolute” timing behaviour of the Crab pulsar is essential.

## Chapter 2

# Instrumentation

In this thesis data collected by the Fermi LAT and XMM Newton EPIC PN instruments have been used. In addition data from INTEGRAL IBIS ISGRI and RXTE PCA have been used as reference material to give a more complete picture.

### 2.1 Fermi LAT

The Large Area Telescope (LAT) is the primary instrument on the Fermi gamma-ray space telescope. It is a wide field-of-view, high-energy gamma-ray telescope. The Fermi gamma-ray space telescope is in a low-Earth orbit at about 565 km and at an inclination of 25.5 degrees. It was launched on the 11<sup>th</sup> of June 2008 and is still operational. The LAT detector is shown in Figure 2.1. The LAT is a pair conversion telescope, converting the incoming gamma-rays into electron-positron pairs which are recorded. The LAT is designed to measure the directions, energies, and arrival times of incident gamma-rays. The LAT has a field-of-view of 2.4 square radians, covers an energy range from below 20 MeV to over 300 GeV, and a timing accuracy of  $<10 \mu\text{s}$ . [6]

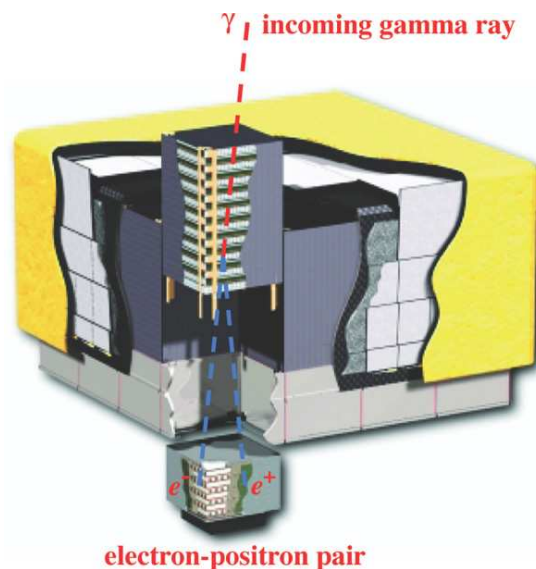


Figure 2.1: The LAT detector, showing an incoming gamma-ray which is converted to an electron-positron pair and recorded by the calorimeter. Source: [6]

## 2.2 XMM Newton EPIC PN

The XMM Newton space telescope carries multiple instruments which makes it sensitive for both X-Ray and optical/UV wavelengths. XMM Newton is in a highly elliptical orbit around Earth with an apogee of about 115000 km and a perigee of about 6000 km. It was launched on the 10<sup>th</sup> of December 1999 and is still operational. The XMM Newton telescope is shown in Figure 2.2. In this thesis I will use data collected with the European Photon Imaging Camera (EPIC), more specifically the EPIC PN camera. This camera is sensitive to photons with energies from 0.15 keV upto 12 keV. The XMM Newton telescope has a field-of-view that is about 30 arcminutes wide. The EPIC PN camera can be used in different modes, the Burst and Timing mode have been used in this thesis. In these modes the time resolution is 7  $\mu$ s and 0.03 ms for the Burst and Timing mode, respectively. [7]

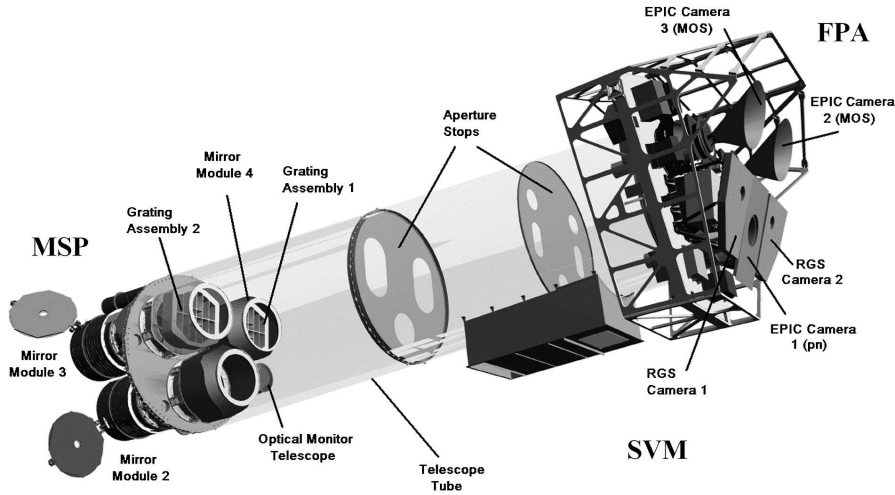


Figure 2.2: XMM Newton space telescope with the mirror modules in the bottom-left corner and the detectors in the top-right corner. Source: [28]

## 2.3 INTEGRAL IBIS ISGRI

The INTEGRAL spacecraft was launched on the 17<sup>th</sup> of October 2002 into a highly elliptical orbit around the Earth. The mission is still operational. IBIS, the Imager on Board the INTEGRAL Satellite (see Figure 2.3), provides fine imaging, source identification, and spectral sensitivity to both continuum and broad lines between 15 keV and 10 MeV. IBIS has a field-of-view of  $29.1^\circ - 29.4^\circ$ . IBIS has two detector planes, ISGRI and PICsIT. In this thesis only data from the ISGRI detector plane is used. The ISGRI detector consists of 8 modules of CdTe pixels, with a total of 16384 pixels. The detector has a timing accuracy of  $61 \mu\text{s}$ . [8]

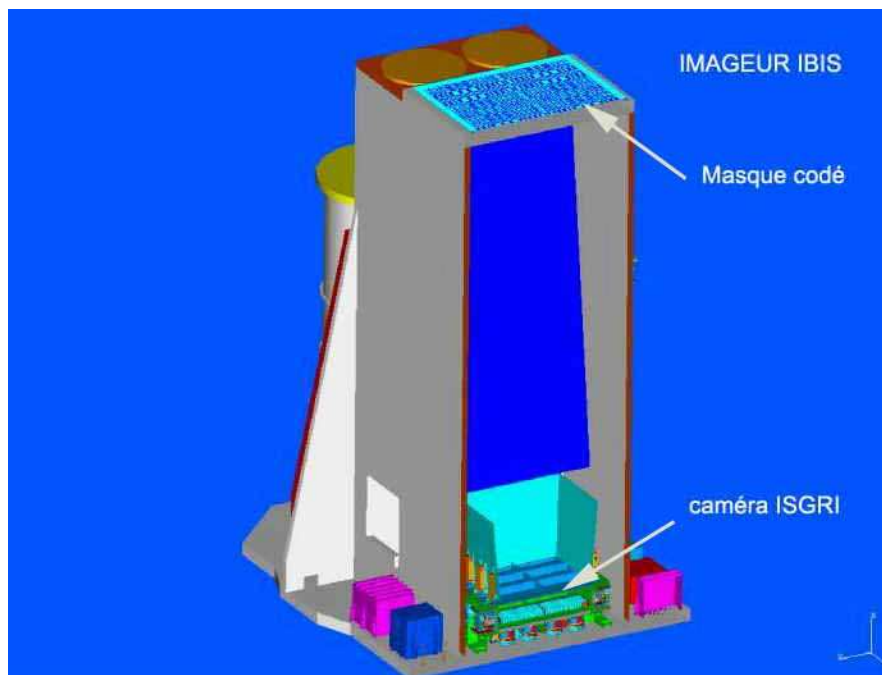


Figure 2.3: A schematic of the IBIS imager. The coded mask is shown at the top of the image and the ISGRI camera with its 8 modules is shown at the bottom. Source: [29]

## 2.4 RXTE PCA

Rossi X-ray Timing Explorer (RXTE) was launched on the 30<sup>th</sup> of December 1995 and was decommissioned on the 5<sup>th</sup> of January 2012. RXTE operated in a low-Earth circular orbit at an altitude of 580 km with an inclination of about 23 degrees. The RXTE spacecraft is shown in Figure 2.4. The Proportional Counter Array (PCA) is one of the instruments on the RXTE spacecraft. The PCA consists of 5 proportional counters, which are gaseous ionisation detectors, and has an energy range from 2 keV up to 60 keV and a time resolution of 1  $\mu$ s. [9] [10]

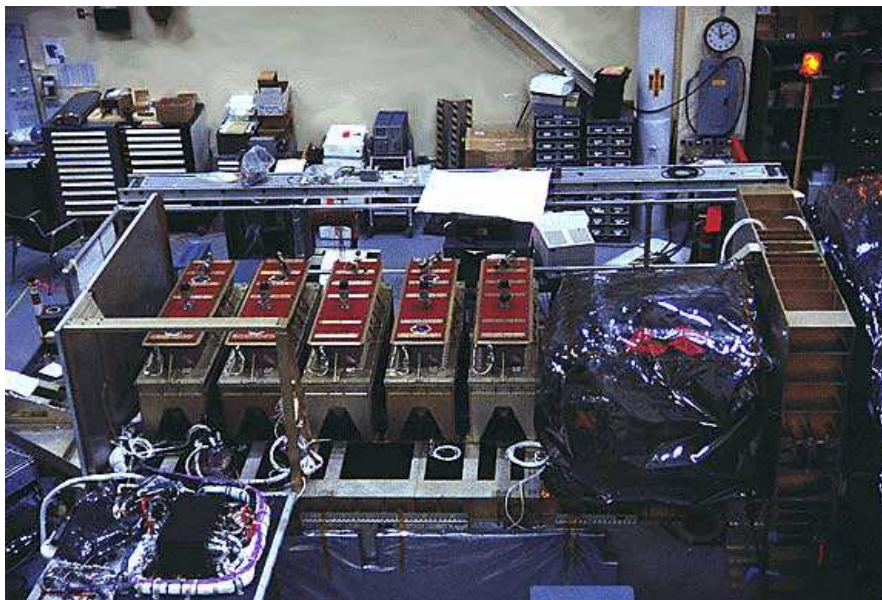


Figure 2.4: The RXTE spacecraft during assembly. The PCA detectors are the 5 identical rectangular instruments. Source: [30]

# Chapter 3

## Data analysis

In this bachelor thesis raw data from the XMM Newton telescope and Fermi LAT telescope have been processed to obtain the “absolute” timing profile of the Crab pulsar. These data as well as the “absolute” timing data from IBIS ISGRI and RXTE PCA have been analysed further to obtain the mean “absolute” time shifts, errors, standard deviations, and to test normality of the obtained distributions. The Jodrell Bank Observatory monthly Crab pulsar ephemerides have served as a baseline for all the data analysed in this bachelor thesis.

### 3.1 The Jodrell Bank Observatory monthly Crab pulsar ephemerides

The Jodrell Bank Observatory (JBO) provides monthly Crab pulsar ephemerides. For monthly validity intervals the ephemerides contain up-to-date parameters of the rotation frequency and its first two time derivatives. These up-to-date parameters are essential for the data analysis in this bachelor thesis because they form the baseline for the performed analysis. The parameters are used in the phase folding step (see Section 3.3.1) in the data analysis. The Crab pulsar ephemerides are derived using radio telescopes of the Jodrell Bank Observatory. The arrival time of radio signals is influenced by dispersion. Therefore variations in the dispersion measure (DM) in the interstellar medium have an impact on the accuracy of the parameters determined in the Jodrell Bank Observatory ephemerides. Glitches also affect the accuracy of these ephemerides.

### 3.2 Preparation for timing analysis

#### 3.2.1 XMM Newton EPIC PN raw data processing

The raw data from XMM Newton EPIC PN needs some processing before timing analysis can be performed. This initial processing of data is done using the Science Analysis Software (SAS) developed for the analysis of XMM Newton data. The first step in the data analysis is the pipeline processing of the raw data. This process transforms the raw data into a format that is required for further scientific research. The pipeline process produces event files including the EPIC PN timing events data, the "`*TimingEvts.ds`" files. These files can be produced for both Burst and Timing mode and contain the relevant data for this bachelor thesis. [12]

### 3.2.2 Barycentering

Barycentering is the process that calculates the arrival time of the events for a fictitious observer in the centre of mass of the Solar System. The barycentre reference frame is the best inertial reference frame in the Solar System. All the data in this bachelor thesis is barycentered using the JPL DE200 planetary ephemeris, the position of the Crab pulsar ( $\alpha_{2000}, \delta_{2000}$ ) which is ( $05^h 34^m 31.97232^s$ ,  $+22^h 00^m 52.0690^s$ ) [19], and the instantaneous positions of the spacecrafts relative to the Earth.

The XMM Newton data is barycentered using the `barycen` program in the SAS package. The Fermi LAT data have been barycentered using the `gtbary` tool provided by the NASA Fermi Science Support Center.[12][13][14]

## 3.3 Timing analysis

Through the timing analysis the measured delay in the arrival time of the Crab pulsar events with respect to the events in radio frequencies is calculated. In this timing analysis the “absolute” time delay of each observation (or part of an observation) is determined. There are a few important steps in this analysis. The first important step is phase folding the data. This process produces pulse-phase distributions by transforming the signal from the time domain to the phase domain (see Equation 3.1) and sampling the phase distribution of an observation. The next step in the analysis is determining the phase shift of the signal compared to the radio frequencies of which the maximum is at phase 1. The delay is then measured by determining the phase of the maximum intensity measured by the instrument and subtracting the phase of the maximum intensity in the radio signal. The phase delay can then be transformed to the time delay. The data of the time delays for each observation of each instrument can be combined in a distribution of time delays versus the time of the observations. Some statistical analysis is performed on these distributions to determine the mean “absolute” time shift for each instrument and to test normality of the distributions.

### 3.3.1 Phase folding

The first step of phase folding is converting the data from the time domain to the phase domain. This is done using the parameters in the Jodrell Bank Observatory monthly Crab pulsar ephemerides. The rotation parameters relate the time domain to the phase domain through the relation in Equation 3.1. This formula is a truncated Taylor series, an approximation using only the rotation frequency  $\nu$  and its first two time derivatives  $\dot{\nu}$ ,  $\ddot{\nu}$ , as well as the phase offset at the epoch  $t_0$  of each ephemeris  $\Phi_0$ .

$$\Phi(t) = \nu \cdot (t - t_0) + \frac{1}{2} \dot{\nu} \cdot (t - t_0)^2 + \frac{1}{6} \ddot{\nu} \cdot (t - t_0)^3 - \Phi_0 \quad (3.1)$$

The individual phases are then sampled and stacked to obtain a pulse-phase distribution. This is done by removing the irrelevant integer part of the phase of every event and sorting the events further according to their fractional part of the phase. The distributions are binned in 360 bins per cycle for the data of Fermi LAT, XMM Newton EPIC PN, and RXTE PCA. The distributions for INTEGRAL IBIS ISGRI are binned in 720 bins per cycle. [15]

### 3.3.2 Cross-correlation of lightcurves

The next step in the analysis is the determination of the phase shift of the signal compared to the radio profile. The maximum intensity of the pulse at radio frequencies is at phase zero. The phase shift of the signal is measured relative to a high statistics template histogram. The “absolute” phase shift of this template has been determined with IDL tools developed by my supervisor, applying a truncated Fourier series to fit the data, of which the maximum is determined.

The shift of each (observation) pulse-phase distribution is then compared to the template through cross-correlation. The errors in this cross-correlation process are determined using Monte Carlo simulations. This method takes into account the whole shape of the lightcurves, not only the maxima of the histograms. This method can accurately determine the relative shift of the data compared to the template lightcurve. This phase shift can then be converted to a time shift to find the “absolute” delay of the pulse-phase distribution of the observation in question.

### 3.4 Statistical analysis of distributions

A statistical analysis has been performed for each instrument on the distribution (of time delays versus the time of the observations) to determine the average “absolute” time shift for each instrument. The mean “absolute” time shift is given by the weighted mean ( $\bar{x}$ ) with a standard deviation ( $\sigma$ ) and a statistical error ( $\sigma_{\bar{x}}$ ). In these equations  $n$  is the number of datapoints in the distribution,  $x_i$  is the value of the  $i^{\text{th}}$  datapoint, and  $w_i$  is the weight of the  $i^{\text{th}}$  datapoint, which depends on the uncertainty of the datapoint ( $\sigma_i$ ). These formulas are given in Equations 3.2 to 3.4:

$$\bar{x} = \frac{\sum_{i=1}^n x_i w_i}{\sum_{i=1}^n w_i}, \quad w_i = \frac{1}{\sigma_i^2} \quad (3.2)$$

$$\sigma = \sqrt{\frac{1}{n-1} \sum_{i=1}^n (x_i - \bar{x})^2} \quad (3.3)$$

$$\sigma_{\bar{x}} = \sqrt{\frac{1}{\sum_{i=1}^n w_i}} \quad (3.4)$$

#### 3.4.1 Skewness and kurtosis

To test normality, the Skewness ( $\mathcal{S}$ ) and Kurtosis ( $\mathcal{K}$ ) and their standard errors, assuming an underlying normal distribution,  $\sigma_{\mathcal{S}}$  and  $\sigma_{\mathcal{K}}$ , respectively have also been determined. The definition of these statistics is given below, in Equations 3.5 to 3.8 [16].

$$\mathcal{S} = \frac{1}{n} \frac{\sum_{i=1}^n (x_i - \bar{x})^3}{\sigma^3} \quad (3.5)$$

$$\sigma_{\mathcal{S}} = \sqrt{\frac{6n(n-1)}{(n-2)(n+1)(n+3)}} \quad (3.6)$$

$$\mathcal{K} = \frac{1}{n} \frac{\sum_{i=1}^n (x_i - \bar{x})^4}{\sigma^4} - 3 \quad (3.7)$$

$$\sigma_{\mathcal{K}} = \sqrt{\frac{24n(n-1)^2}{(n-3)(n-2)(n+3)(n+5)}} \quad (3.8)$$

The skewness and kurtosis are both zero for a normal distribution. Skewness determines the asymmetry due to the tails of the distribution. A positive value for  $\mathcal{S}$  means a tail that is more prominent at positive x-values. A negative value signifies a tail that is more prominent at negative x-values. Kurtosis determines the relative heavy-tailedness or weak-tailedness of the distribution compared to a normal distribution. Negative kurtosis and positive kurtosis signify light-tailedness and heavy-tailedness, respectively. [17]

# Chapter 4

## Results

I analysed the data from Fermi LAT and XMM Newton collected from August 2008 and February 2000, respectively, up to October 2016. This analysis further updates the existing picture of “absolute” timing of the Crab pulsar derived using the INTEGRAL IBIS ISGRI and RXTE PCA instruments. The values for the time shift, uncertainties, and standard deviations of the distributions are given in Table 4.1 accompanied by other statistical values, such as skewness, kurtosis, and the number of measurements.

During this work some of the delay measurements showed (suspicious) deviant behaviour from their predicted values. We call these measurements outliers. Table 4.2 gives a list of all the measurements classified as outliers and the reason for this classification. The “absolute” timing picture of the Crab pulsar is visualised in Figures 4.1 and 4.2 with and without outliers, respectively. In the following sections I will discuss the obtained distributions, statistical values, and outliers in more detail.

<b>Instrument</b>	$\tau$ ( $\mu s$ )	$\Delta\tau$ ( $\mu s$ )	$\sigma$ ( $\mu s$ )	$\mathcal{S}$	$\mathcal{K}$	<b>n</b>
Fermi LAT						
<i>With outliers</i>	-104	$\pm 4$	$\pm 88$	$1.4 \pm 0.2$	$3.8 \pm 0.5$	107
<i>Without outliers</i>	-111	$\pm 4$	$\pm 57$	$0.5 \pm 0.3$	$0.2 \pm 0.5$	93
XMM Newton EPIC PN						
<i>Burst mode</i>	-353	$\pm 4$	$\pm 75$	$-0.1 \pm 0.3$	$-0.6 \pm 0.7$	43
<i>Timing mode</i>	-271	$\pm 4$	$\pm 69$	$0.1 \pm 0.4$	$-0.3 \pm 0.7$	42
<i>Burst + Timing mode</i>	-312	$\pm 3$	$\pm 83$	$-0.1 \pm 0.3$	$-0.3 \pm 0.5$	85
INTEGRAL IBIS ISGRI						
<i>With outliers</i>	-245	$\pm 2$	$\pm 76$	$0.5 \pm 0.2$	$1.2 \pm 0.4$	122
<i>Without outliers</i>	-248	$\pm 2$	$\pm 61$	$0.1 \pm 0.2$	$-0.7 \pm 0.5$	112
RXTE PCA						
<i>With outliers</i>	-288	$\pm 3$	$\pm 79$	$2.0 \pm 0.2$	$7.7 \pm 0.3$	205
<i>Without outliers</i>	-297	$\pm 3$	$\pm 56$	$0.1 \pm 0.2$	$1.5 \pm 0.3$	197

Table 4.1: Time shift ( $\tau$ ), uncertainty ( $\Delta\tau$ ), standard deviation of the distribution ( $\sigma$ ), skewness ( $\mathcal{S}$ ), kurtosis ( $\mathcal{K}$ ) and the number of measurements (n).

Observation time (MJD)	JBO ephemeris	Reason for classification as outlier
<b>Fermi LAT</b>		
55257 - 55287 (4 observations)	March 2010	Quadratic trend, probable error in $\dot{\nu}$ of JBO ephemeris
55287 - 55317 (4 observations)	April 2010	Linear trend, probable error in $\nu$ of JBO ephemeris
55348 - 55379	June 2010	Constant offset, probable shift or error in $\Phi_0$ of JBO ephemeris
55823 - 55839	2/2 September 2011	Increased dispersion measure, JBO note 27 [19]
55876 - 55883	2/3 November 2011	A glitch on MJD 55785, JBO note 28 [19]
<b>XMM Newton Burst mode</b>		
51600.9	February 2000	Significantly phase shifted, ignored in analysis.
56721.8	May 2014	Significantly phase shifted, ignored in analysis.
<b>XMM Newton Timing mode</b>		
56720.8	May 2014	Significantly phase shifted, ignored in analysis.
<b>INTEGRAL IBIS ISGRI</b>		
53654.59	October 2005	Linear trend, probable error in $\nu$ of JBO ephemeris
53673.78	October 2005	Linear trend, probable error in $\nu$ of JBO ephemeris
55259.22	March 2010	Quadratic trend, probable error in $\dot{\nu}$ of JBO ephemeris
55262.85	March 2010	Quadratic trend, probable error in $\dot{\nu}$ of JBO ephemeris
55290.41	April 2010	Linear trend, probable error in $\nu$ of JBO ephemeris
55294.74	April 2010	Linear trend, probable error in $\nu$ of JBO ephemeris
55297.71	April 2010	Linear trend, probable error in $\nu$ of JBO ephemeris
55300.67	April 2010	Linear trend, probable error in $\nu$ of JBO ephemeris
55303.68	April 2010	Linear trend, probable error in $\nu$ of JBO ephemeris
57451.75	March 2016	Phase shifted
<b>RXTE PCA</b>		
53342	December 2004	Constant offset, probable error in $\Phi_0$ of JBO ephemeris
53356	December 2004	Constant offset, probable error in $\Phi_0$ of JBO ephemeris
53370	December 2004	Constant offset, probable error in $\Phi_0$ of JBO ephemeris
55269	March 2010	Quadratic trend, probable error in $\dot{\nu}$ of JBO ephemeris
55281	March 2010	Quadratic trend, probable error in $\dot{\nu}$ of JBO ephemeris
55295	April 2010	Linear trend, probable error in $\nu$ of JBO ephemeris
55312	April 2010	Linear trend, probable error in $\nu$ of JBO ephemeris

Table 4.2: List of all the measurements classified as outliers. The causes of the trends in the outliers are discussed in Section 4.2.2.

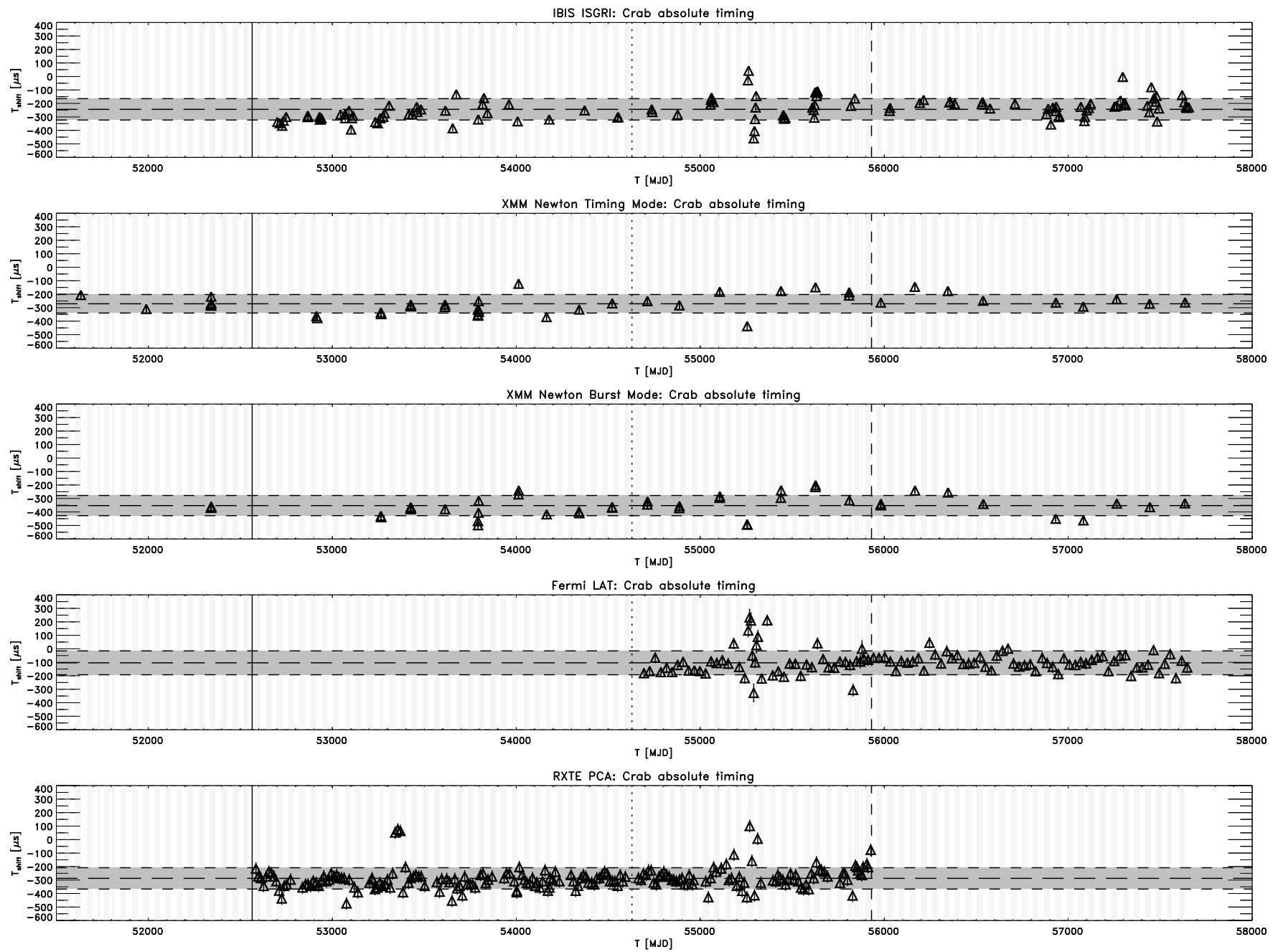


Figure 4.1: Crab pulsar “absolute” timing with IBIS ISGRI, XMM Newton (Timing and Burst mode), Fermi LAT, and RXTE PCA. Outliers have not been removed from this data. The solid vertical line shows the launch date of INTEGRAL, the short-dashed line shows the launch date of Fermi LAT, and the long-dashed line shows the date on which RXTE PCA was decommissioned. The alternating light grey and white vertical stripes show the different JBO ephemerides.

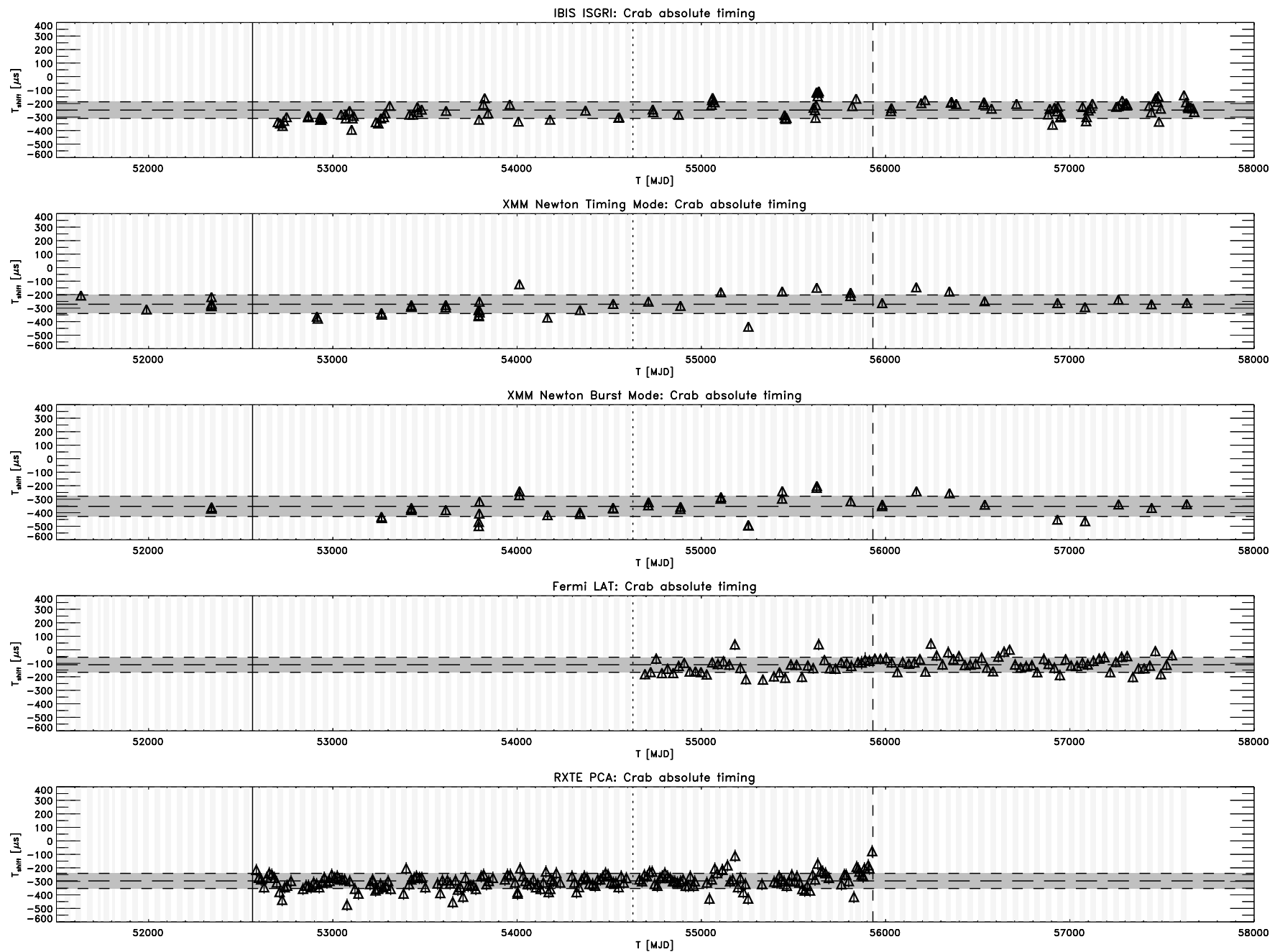


Figure 4.2: Crab pulsar “absolute” timing with IBIS ISGRI, XMM Newton (Timing and Burst mode), Fermi LAT, and RXTE PCA. Outliers have been removed from this data. The solid vertical line shows the launch date of INTEGRAL, the short-dashed line shows the launch date of Fermi LAT, and the long-dashed line shows the date on which RXTE PCA was decommissioned. The alternating light grey and white vertical stripes show the different JBO ephemerides.

## 4.1 “Absolute” timing distributions

### 4.1.1 Fermi LAT

The Fermi LAT telescope has observed the Crab pulsar continuously since August 2008. The data has been phase folded between the start and end date of each entire JBO ephemeris validity interval. This means that there is one datapoint for each JBO ephemeris. Only for a few months I made an exception and split up some of the monthly data to visualise possible trends within a single ephemeris period. This has been done for the months March and April in 2010. The corresponding datapoints are flagged as outliers. There are in total 11 outliers in the LAT measurements. The histogram in Figure 4.3 shows the impact of these outliers on the distribution of the data. With the outliers included the distribution is slightly skewed to the right and heavily tailed, which can be deduced from the values of skewness and kurtosis in Table 4.1. Without the outliers the distribution is normally distributed.

Analysis of the Fermi LAT data resulted in an average time shift of  $-111 \pm 4 \mu\text{s}$  with a standard deviation of  $\pm 57 \mu\text{s}$ , excluding outliers. In this result the statistical error is reported. The VERITAS collaboration (2011) reported a value of  $-138 \pm 12 \pm 21 \mu\text{s}$  [21], where the first uncertainty in this value is due to statistics and the second arises from systematics. This value is consistent at a 95% confidence level with the value of  $-141 \pm 34 \mu\text{s}$  that we obtained over roughly the same time period (Aug. 2008 - Apr. 2009).

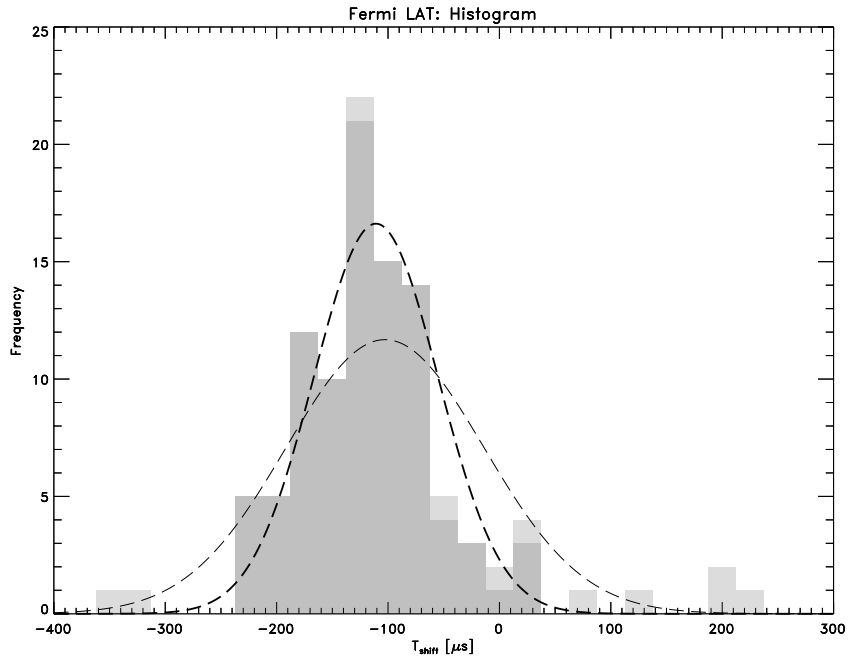
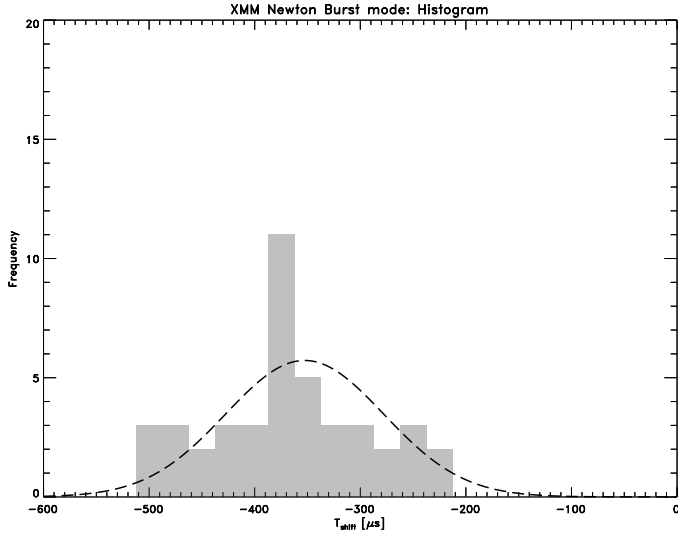


Figure 4.3: Fermi LAT “absolute” timing distribution histogram without outliers in dark grey and outliers in light grey. The thick and thin dashed lines are the Gaussian functions for the distributions without and with outliers, respectively. The binsize is  $25 \mu\text{s}$ .

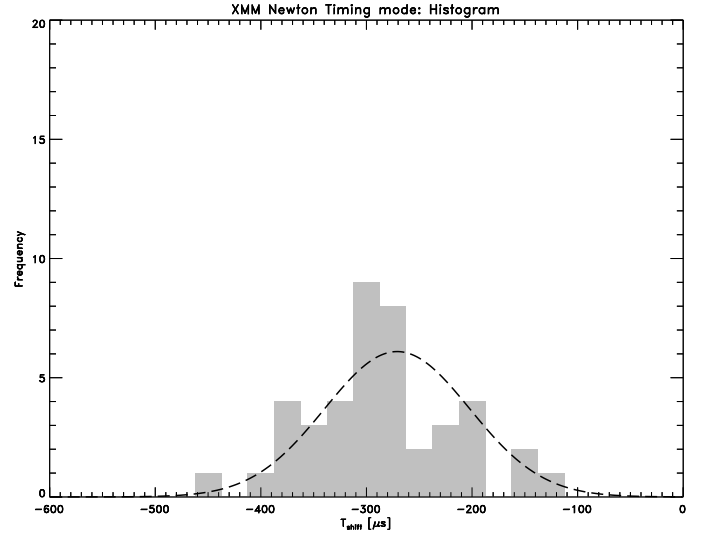
### 4.1.2 XMM Newton EPIC PN

The analysed XMM Newton data originated from two operational modes, the Burst and Timing mode. The timing data for these modes have been phase folded for each entire (short duration) observation. Therefore there is one datapoint for each observation. The total number of observations is small for both modes (see Table 4.1), making it difficult to judge whether these distributions are normally distributed. The skewness and kurtosis are consistent with normal distributions for all three distributions analysed, i.e. the Burst, Timing, and the combination of these modes. Visually, the histogram with the combined data of the modes seems bimodal. Both modes, Burst and Timing mode, have outliers for which there is a significant phase offset. These outliers have been ignored in the data analysis, but are shown in Table 4.2.

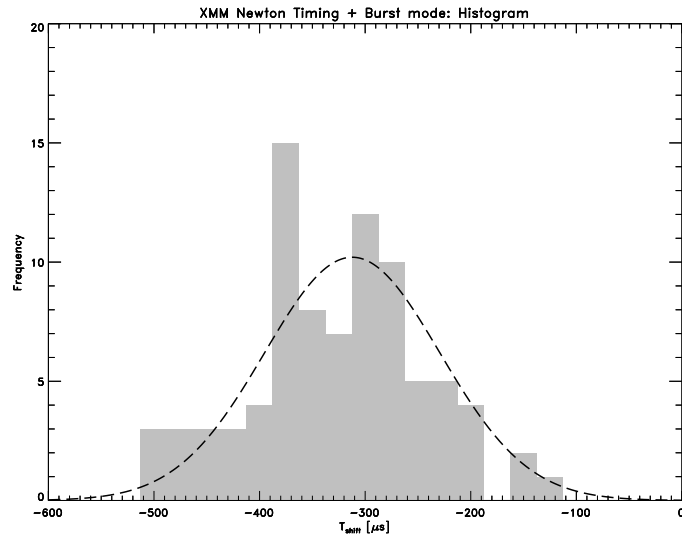
For the Burst mode the timing analysis resulted in an average time shift of  $-353 \pm 4 \mu\text{s}$  with a standard deviation of  $\pm 75 \mu\text{s}$ . The histogram of this distribution is shown in Figure 4.4a. For the Timing mode this resulted in an average time shift of  $-271 \pm 4 \mu\text{s}$  with a standard deviation of  $\pm 69 \mu\text{s}$  (see Figure 4.4b). There is a considerable discrepancy between the “absolute” time shifts of these modes. Analysing the data as a single distribution i.e. Burst and Timing mode combined results in a broader bimodal distribution as can be seen in Figure 4.4c. This broadening is also evident from the standard deviation of this distribution, which is  $\pm 83 \mu\text{s}$ . The value of the measured “absolute” time shift for the combined data of Burst mode and Timing mode is  $-312 \pm 3 \mu\text{s}$ . The “absolute” time shift determined by Martin-Carrillo et al. (2012) is  $-306 \pm 9 \mu\text{s}$ , using 32 XMM-Newton observations in both Burst mode and Timing mode, which is consistent with our result at a 95% confidence level. An updated value is given in the XMM Newton Calibration Technical Note (2015):  $-351 \pm 10 \mu\text{s}$ , mixing the Burst and Timing mode data. This value is inconsistent with the result that we obtained when the Burst and Timing mode data are combined, at a 95% confidence level. The discrepancy between the Burst and Timing mode results show that the data from these modes should not be mixed, but analysed separately.



(a) XMM Newton EPIC PN Burst mode



(b) XMM Newton EPIC PN Timing mode



(c) XMM Newton EPIC PN Burst + Timing mode

Figure 4.4: XMM Newton EPIC PN “absolute” timing distribution histograms in dark grey. The dashed lines are the Gaussian functions of the distributions. The binsize is  $25 \mu\text{s}$ . The top-left shows the histogram of only Burst mode data, the top-right shows the histogram of only Timing mode data. The bottom histogram shows a histogram of the mixed Burst mode and Timing mode data.

### 4.1.3 INTEGRAL IBIS ISGRI

Timing data from each individual observation of INTEGRAL IBIS ISGRI has been phase folded and forms one datapoint. There are 10 outliers in the data for INTEGRAL IBIS ISGRI. The outliers have a small broadening effect on the shape of the distribution. The distribution with outliers is slightly skewed to the right and heavy-tailed, as can be deduced from the values of skewness and kurtosis in Table 4.1. The distribution without outliers is nearly normally distributed, judging the skewness and kurtosis, but visually it seems to be slightly bimodal.

The INTEGRAL IBIS ISGRI timing data (without outliers) resulted in an average time shift of  $-248 \pm 2 \mu\text{s}$  (statistical error only) with a standard deviation of  $\pm 61 \mu\text{s}$ . The “absolute” time shift for INTEGRAL IBIS ISGRI had been determined earlier by Kuiper et al. (2003) at  $-285 \pm 12 \mu\text{s}$ . This value should be corrected for a general (REDU) ground station delay of  $47 \mu\text{s}$ , unknown at the beginning of the mission. The corrected value is  $-238 \pm 12 \mu\text{s}$ , which is consistent with the measured value at a 95% confidence level.

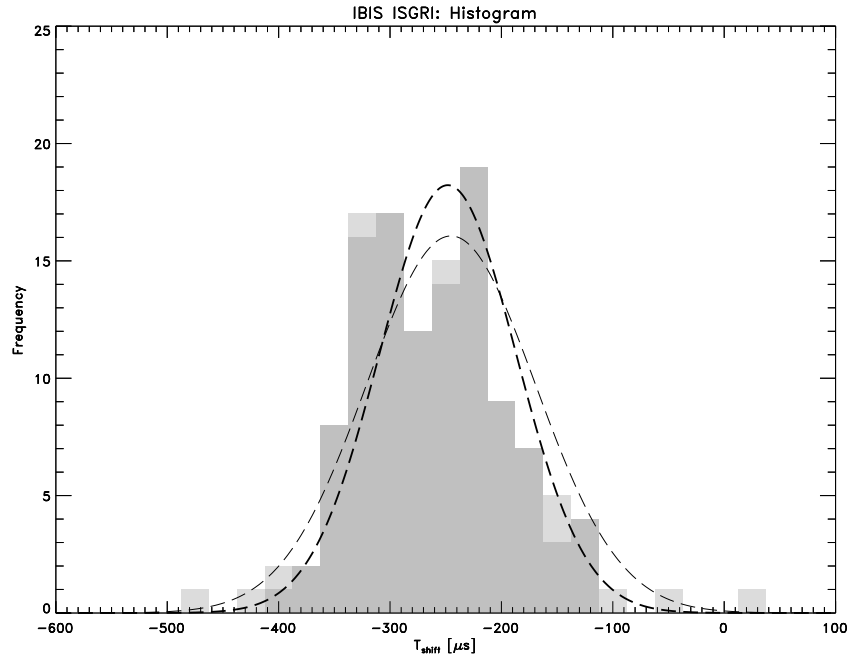


Figure 4.5: INTEGRAL IBIS ISGRI “absolute” timing distribution histogram without outliers in dark grey and outliers in light grey. The thick and thin dashed lines are the Gaussian functions for the distributions without and with outliers, respectively. The binsize is  $25 \mu\text{s}$ .

#### 4.1.4 RXTE PCA

Timing data from each individual RXTE PCA observation has been phase folded to form one datapoint. There are 7 outliers in the RXTE PCA data. Most of these outliers are due to likely uncertainties in JBO ephemerides. These outliers have a small broadening effect on the shape of the distribution. The distribution with outliers is skewed to the right and light-tailed. The distribution without outliers is not skewed but is still light-tailed (see Figure 4.6).

Analysis of the RXTE PCA timing data (without outliers) resulted in an average time shift of  $-296 \pm 3 \mu\text{s}$  with a standard deviation of  $\pm 56 \mu\text{s}$ . The “absolute” time shift for RXTE PCA has been determined earlier by Rots et al. (2004) at  $-344 \pm 5 \pm 40 \mu\text{s}$ , where the first uncertainty is the statistical uncertainty and the second is a systematical uncertainty. Taking both uncertainties into account this result is consistent with the value that I measured at a 95% confidence level. The time shift has also been determined by Molkov et al. (2010) at  $-310 \pm 6 \mu\text{s}$ , which is also consistent with our measurement at a 99% confidence level. These values have been obtained using different techniques and different datasets. The results published by Rots et al. (2004) have been determined using an asymmetric Lorentzian to fit the maximum of the pulse-phase profiles to determine the phase shift. The results published by Molkov et al. (2010) have been determined by fitting two asymmetric Lorentzians to the maximum of the pulse and the interpulse of the pulse-phase profiles to determine the phase shift. The method used in this bachelor thesis uses the shape of the whole profile with a truncated Fourier series of which the maximum is determined.

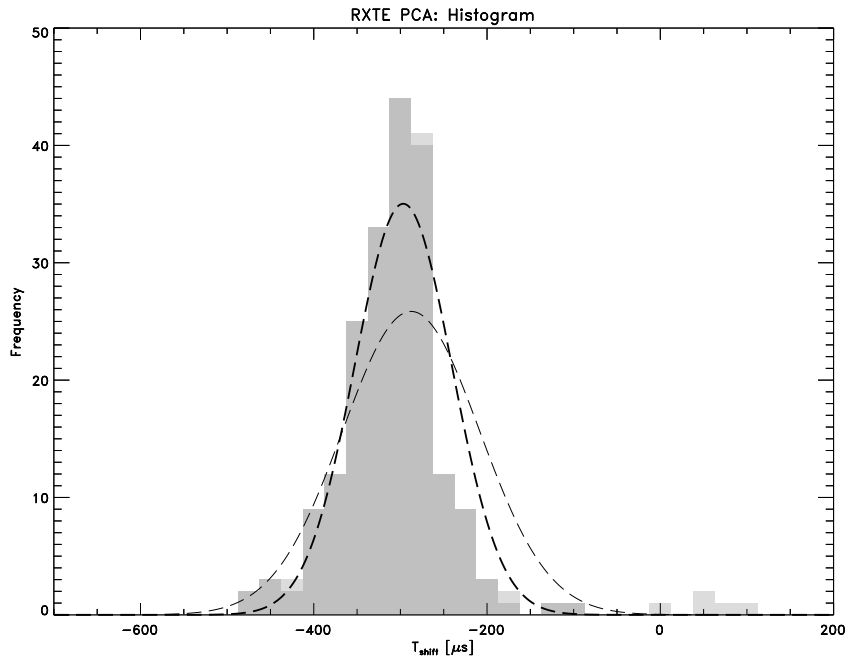


Figure 4.6: RXTE PCA “absolute” timing distribution. Histogram without outliers in dark grey and outliers in light grey. The thick and thin dashed lines are the Gaussian functions for the distributions without and with outliers, respectively. The binsize is  $25 \mu\text{s}$ .

## 4.2 JBO monthly ephemerides of the Crab pulsar

The JBO Crab pulsar monthly ephemerides[18] have been a key part in this “absolute” timing study. The monthly ephemerides have served as a baseline for all the timing measurements.

### 4.2.1 Uncertainty in the ephemerides

The standard deviation ( $\sigma_M$ ) of the measured “absolute” timing distributions shows the combined, quadratically added, of the instrument dependent error ( $\sigma_I$ ) and of the JBO ephemeris dependent error ( $\sigma_{JBO}$ ). This relation is expressed in Equation 4.1:

$$\sigma_M^2 = \sigma_I^2 + \sigma_{JBO}^2 \quad (4.1)$$

As shown in Table 4.1, the standard deviations ( $\sigma_M$ ) of the time shift distributions (without outliers) are on the order of  $\pm 60 \mu s$  for Fermi LAT, IBIS ISGRI, and RXTE PCA and only slightly higher for the XMM Newton distributions. The JBO monthly ephemerides provide an uncertainty measure,  $t_{acc}$  [31], for every ephemeris. The distribution of this value is shown in Figure 4.7 including 209 ephemeris entries, 14 of which have been classified as outliers (light grey). Outliers are defined here as those ephemerides for which we discovered trends in the high-energy data or ephemerides with an uncertainty higher than  $300 \mu s$ . The mean of the distribution excluding outliers is  $118 \mu s$  with a standard deviation of  $43 \mu s$ .

We are still waiting for feedback from JBO scientists on the confidence level of this uncertainty measure  $t_{acc}$ . A one sigma confidence level for  $t_{acc}$  is excluded due to the smaller spreads in the measured “absolute” timing values. Assuming a two sigma confidence level, only a small instrumental uncertainty of 10-20  $\mu s$  would be permitted for Fermi LAT, INTEGRAL IBIS ISGRI, and RXTE PCA. This value is slightly higher for the XMM Newton EPIC PN due to the larger spread in the timing data.

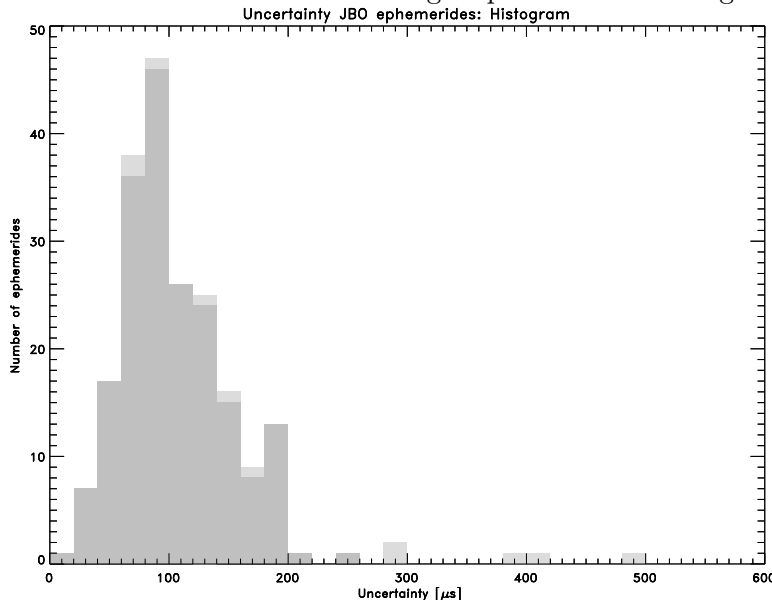


Figure 4.7: A histogram of the uncertainty  $t_{acc}$  in JBO monthly Crab pulsar ephemerides. Uncertainties without outliers are coloured dark-grey. Outliers are colored light grey. 3 outliers have an uncertainty of more than  $600 \mu s$  and are outside the plot range of this figure.

## 4.2.2 Trends of outliers within ephemerides

During the “absolute” timing analysis I discovered that the outliers in the data were often clustered within the validity interval of the same ephemeris. It is noticeable that some of these clusters of outliers follow certain trends. Some of these trends are suspected to be due to uncertainties in the rotation frequency  $\nu$  and/or its time derivatives  $\dot{\nu}$  and  $\ddot{\nu}$ , or due to a too-far-off phase offset  $\Phi_0$  of the ephemeris provided by the Jodrell Bank Observatory. Some other errors could have been caused by periods of increased dispersion measure variations, glitches, and glitch recovery periods. In this section I will discuss some of the trends in these clusters of outliers.

Errors in these parameters produce trends in the pulse-phase distributions after the phase folding method. This method relies on the accuracy of these parameters. If these parameters are incorrect, then incorrect phases are calculated and the profile will be sampled incorrectly. For example if the phase offset  $\Phi_0$  is too-far-off that will cause all the phases to be too-far-off and therefore the full profile will be too-far-off. If there is an error in the rotation frequency a similar error occurs. This means that over the course of the validity interval of the ephemeris the position of the maximum of the profile shifts linearly. Errors in the derivatives of the rotation frequency cause quadratic (first derivative) or higher order (higher derivatives) trends. These trends have been found in the analysed data.

The first cluster of outliers is located in the ephemeris of December 2004, which is valid between MJD 53341 and 53372. There are only RXTE PCA measurements during this ephemeris. The timing measurements show a constant time shift during this month, which is too-far-off. This constant time shift can be seen in Figure 4.8. This shift could have been caused by an error in determining the phase offset  $\Phi_0$ , which leads to a constant too-far-off offset in the “absolute” timing data. There was a glitch on MJD 53331 [19], which makes it likely that the error is related to the glitch recovery issues.

Other outliers can be found in the ephemeris of October 2005, which is valid between MJD 53644 and 53675. Both INTEGRAL IBIS ISGRI and RXTE PCA have two data-points during this ephemeris, which show a slight slope in the “absolute” timing. This is shown in Figure 4.9. There are insufficient data to show the nature of the trend in this ephemeris, but an error in the rotation frequency of the Crab pulsar is very likely.

More convincing are the trends in the clusters of outliers in the ephemerides of the months March and April of 2010, with validity intervals between MJD 55257-55287 and MJD 55287-55317, respectively. These trends have been observed by the Fermi LAT, IBIS ISGRI, and RXTE PCA instruments. These trends are shown in Figure 4.10. In March 2010 a non-linear trend can be seen in the “absolute” time shift. This non-linear trend seems to have a quadratic profile so it is probably caused by an error in the rotation frequency time derivative  $\dot{\nu}$ . In April 2010 a linearly increasing trend is recorded. This linear trend is probably caused by an error in the rotation frequency of the JBO ephemeris  $\nu$ .

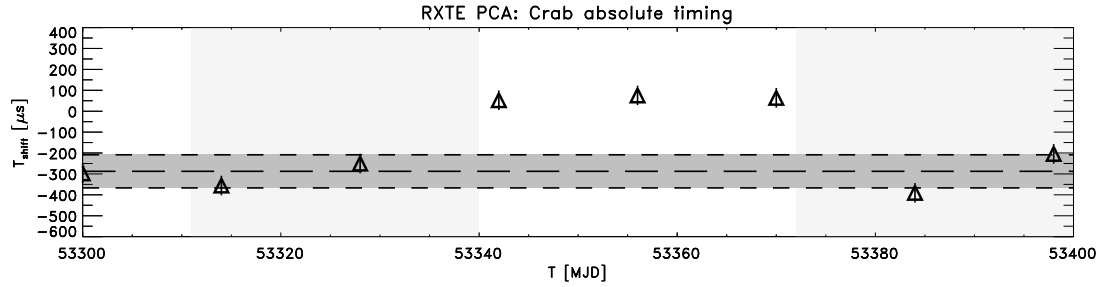


Figure 4.8: Zoom-in of Figure 4.1 for RXTE PCA between MJD 53300 and MJD 53400. JBO ephemerides shown in alternating white and grey. The ephemeris for December 2004 is from MJD 53341 to MJD 53372.

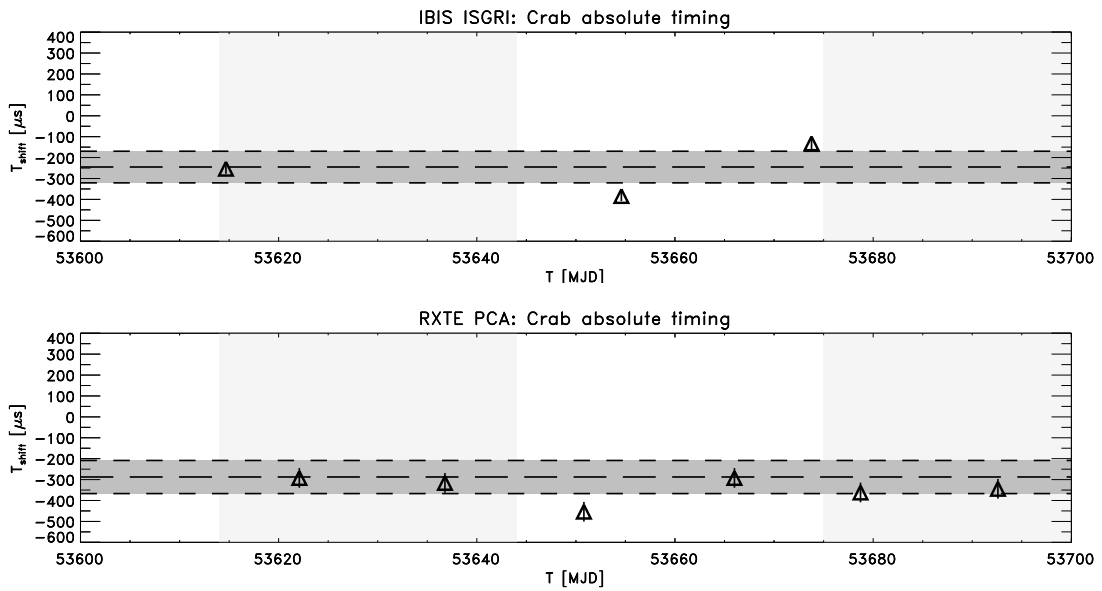


Figure 4.9: Zoom-in of Figure 4.1 for INTEGRAL IBIS ISGRI and RXTE PCA between MJD 53600 and MJD 53700. JBO ephemerides shown in alternating white and grey. The ephemeris for October 2005 is from MJD 53644 to MJD 53675.

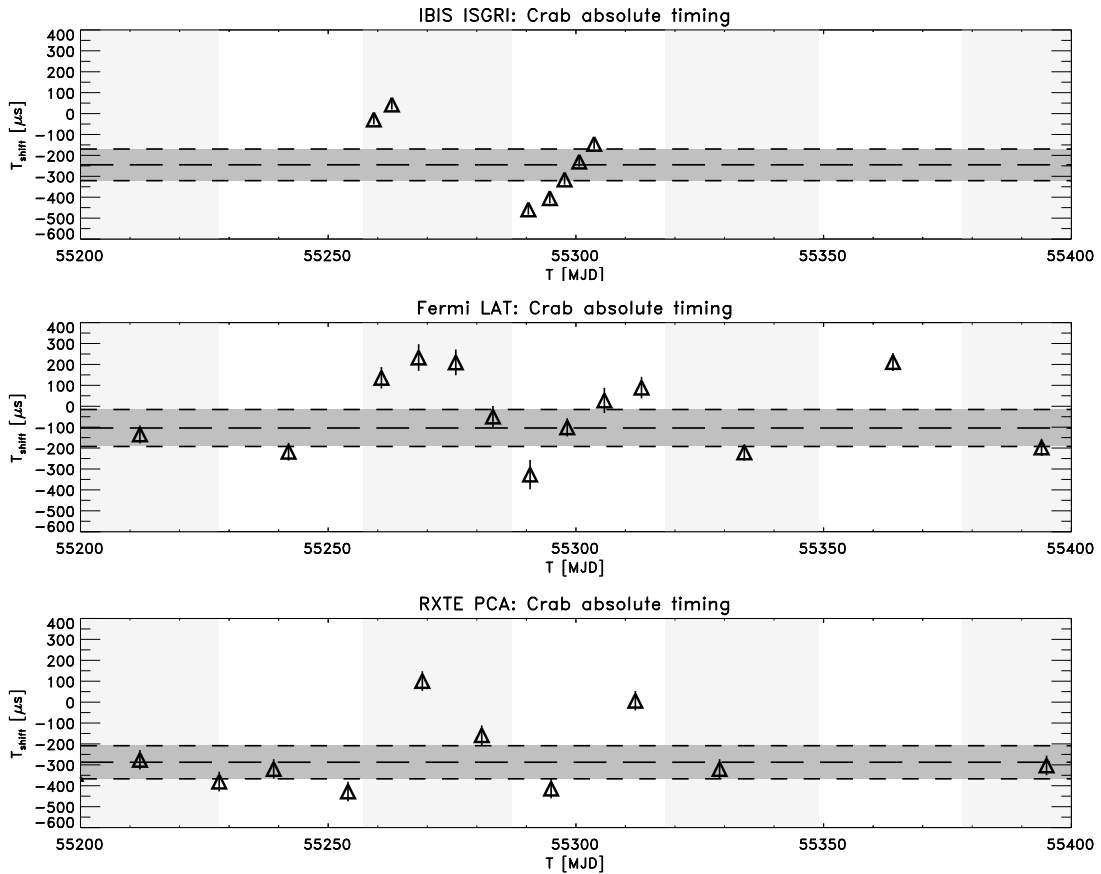


Figure 4.10: Zoom-in of Figure 4.1 for INTEGRAL IBIS ISGRI, Fermi LAT and RXTE PCA between MJD 55200 and MJD 55400. JBO ephemerides shown in alternating white and grey. The ephemeris for March 2010 is from MJD 55257 to MJD 55287 and the ephemeris for April 2010 is from MJD 55287 to MJD 55317.

### 4.3 Radio delay evolution with energy

The “absolute” time shifts determined in this bachelor thesis combined with the updated values for INTEGRAL IBIS ISGRI and RXTE PCA provide information on the relation between the time delay and the energy of the radiation. This relation has been described by Molkov et al.[27] and can be seen in Figure 4.11. Most of the measurements in this figure seem to follow a linear relationship (dashed line Figure 4.11). The radio delay seems to decrease with energy.

The new data obtained for Fermi LAT and INTEGRAL IBIS ISGRI does not follow this linear trend. Fermi LAT has a radio delay of  $-111 \pm 4 \mu\text{s}$  which is too high to follow the linear relation. The relative time shift between IBIS ISGRI measurements at 20-100 keV and 100-300 keV has been determined by my supervisor and turns out to be only  $4.9 \pm 1.4 \mu\text{s}$ , and thus the delay across the full 20-300 keV band is consistent with approximately  $-248 \mu\text{s}$  without any (linearly) decreasing trend.

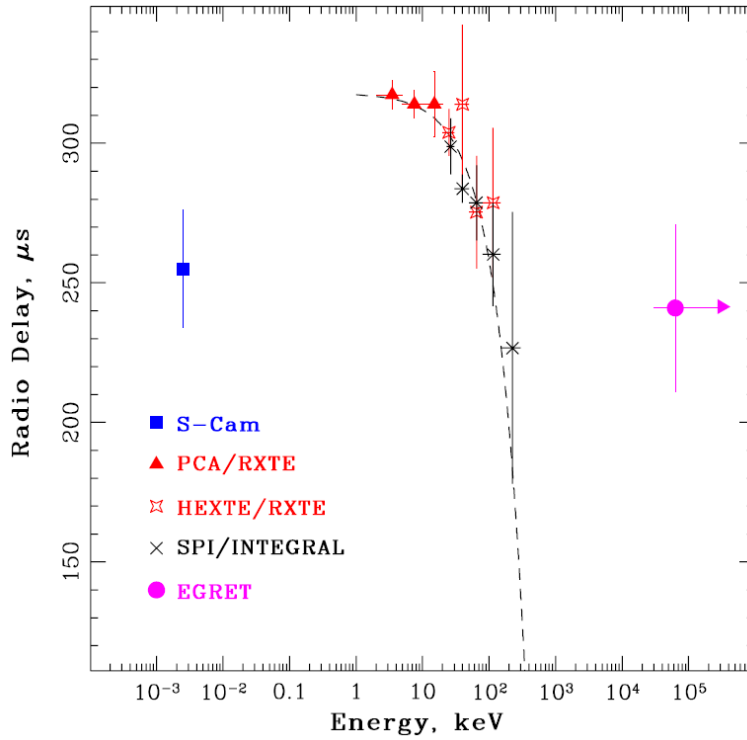


Figure 4.11: Radio delay as a function of energy with the optical (S-Cam), X-ray (RXTE, SPI), and gamma-ray (EGRET) datapoints. The dashed line is a linear relation. Image: Molkov et al. (2010)

## Chapter 5

# Discussion and conclusions

In this bachelor thesis I have updated the high-energy “absolute” timing picture of the Crab pulsar by including the Fermi LAT high-energy gamma-ray data ( $>100$  MeV) collected since the start of the nominal science operations (4-8-2008) until October 2016, and the XMM Newton EPIC PN data by analysing the bi-yearly Crab timing observations taken in Burst and Timing mode (0.3-12 keV). This bachelor thesis also uses the high-energy “absolute” timing data of INTEGRAL IBIS ISGRI (20-300 keV, from launch up to October 2016) and RXTE PCA (3-32 keV, from INTEGRAL launch until its decommissioning). The Jodrell Bank Observatory Crab pulsar monthly ephemerides have served as a baseline for all these “absolute” timing measurements.

The mean “absolute” time shift has been determined at  $-111 \pm 4 \mu\text{s}$  for Fermi LAT. The Fermi LAT data have been a useful tool in finding possible errors in the Jodrell Bank Observatory Crab pulsar monthly ephemerides because of its continuous observation of the Crab pulsar in all-sky survey mode. This makes it possible to further analyse months where there are possible increased uncertainties in the baseline. This is done by splitting the observation interval up into several shorter intervals to visualise the trend within the observation. This strategy has been used for the months March and April of 2010.

For XMM Newton EPIC PN two operational modes have been analysed, Burst mode and Timing mode. The mean “absolute time shifts for XMM Newton EPIC PN Burst and Timing mode have been determined at  $-353 \pm 4 \mu\text{s}$  and  $-271 \pm 4 \mu\text{s}$ , respectively. These values show that there is a discrepancy between the measured “absolute” time shift of these modes. Therefore the data from these modes should be analysed separately. Mixing the data resulted in a broader and bimodal distribution. Analysing the XMM Newton data also revealed some problems with frame jumps. Some of these frame jumps could be corrected by the SAS software, but others remained and these observations could not be used.

The “absolute” time shifts from INTEGRAL IBIS ISGRI and RXTE PCA have been determined at  $-248 \pm 2 \mu\text{s}$  and  $-297 \pm 3 \mu\text{s}$ , respectively. The value for INTEGRAL IBIS ISGRI is consistent with the value determined by Kuiper et al. (2003) after correcting this number by a  $47 \mu\text{s}$  general delay found later during the mission. The value for RXTE PCA is consistent with the values determined by Rots et al. (2004) and Molkov et al. (2010).

The Jodrell Bank Observatory Crab pulsar monthly ephemerides have been the baseline for all the measurements that have been made in this bachelor thesis, therefore it has been of great significance. In almost all observations the ephemerides have demonstrated to be very reliable. Only in a few cases some possible errors have been found in the rotation parameters specified in the ephemerides. These suspected errors produced trends in the “absolute” timing data of the instruments. An error in the baseline is suspected when these trends have been measured simultaneously in multiple instruments.

An important advantage of using the data from the high-energy instruments is that at these energies no effects due to DM variations are present. The radio measurements of the Jodrell Bank Observatory are influenced by the dispersion measure, which adds considerably to the uncertainty in the timing measurements. The dispersion measure could in principle be accurately determined by a joint analysis of radio frequency data and high-energy data to accurately determine the rotation frequency and time derivatives of the Crab pulsar.

The measured standard deviations ( $\sigma_M$ ) of the “absolute” time shift in combination with the uncertainty measure on radio pulse arrival times  $t_{acc}$  provided by the Jodrell Bank Observatory make it possible to give a rough estimate of the instrument uncertainties ( $\sigma_I$ ). We are still waiting for feedback on the confidence level of the uncertainty  $t_{acc}$ . Assuming a two sigma confidence level for  $t_{acc}$ , only a small instrumental uncertainty would be permitted for the analysed instruments.

This bachelor thesis does not support the linear relation between the “absolute” time shift and the energy of the radiation that has been given by Molkov et al. (2010). The new data that have been obtained in this study do not follow the linear model (Figure 4.11) that Molkov et al. (2010) proposed.

The “absolute” timing study in this work contains “absolute” timing analysis over a period of time longer than has been analysed before for the analysed instruments. Due to this long term analysis the statistical uncertainties in the mean “absolute” time shift have been reduced and the picture of the “absolute” timing of the Crab pulsar for high-energy instruments has been updated. The Fermi, INTEGRAL, and XMM Newton instruments are still operational and thus the picture can be further expanded by adding future observations. Continued “absolute” timing analysis of these data could also be used as a tool to examine the reliability of Jodrell Bank Observatory Crab pulsar ephemerides that have been produced after September 2016.

## Chapter 6

# Acknowledgement

I am very glad to have been able to write my bachelor thesis at SRON Netherlands Institute for Space Research. It has given me a glimpse of doing research in astrophysics. I would like to express my special thanks to Dr. Lucien Kuiper for being my supervisor, for making it possible for me to write my bachelor thesis at SRON, and for always being available for advice and help. I would also like to thank Dr. Enrico Pajer for making this bachelor thesis possible by being my contact person at Utrecht University.

# Bibliography

- [1] NASA. (2002) *Astronomy Picture of the Day*. [online] Available at: <http://apod.nasa.gov/apod/ap020920.html> [Accessed Dec. 2016]
- [2] Ryden, B. and Peterson, B. (2012). *Foundations of Astrophysics*. International ed. Cambridge: Cambridge University Press, pp. 393-431
- [3] Lyne, A. et al. (2014). 45 Years of Rotation of the Crab pulsar. *Monthly Notices of the Royal Astronomical Society*, 1(9), pp. 1-5
- [4] Lyne, A. and Graham-Smith, F. (2012) *Pulsar Astronomy*. Fourth ed. Cambridge: Cambridge University Press, pp. 61-75, 118-128, 258-277
- [5] Martin-Carrillo, A. et al. (2012). The relative and absolute timing accuracy of the EPIC-pn camera on XMM-Newton, from X-ray pulsations of the Crab and other pulsars. *Astronomy & Astrophysics*, 545(A126), pp. 1-11 A&A 545, A126 (2012).
- [6] Atwood, W. et al. (2009). The Large Area Telescope on the Fermi Gamma-ray Space Telescope Mission. *The Astrophysical Journal*, 697, pp.1071-1102
- [7] ESA:XMM-Newton SOC. (2013). *XMM-Newton Users Handbook*, 1(2.11) [online] Available at: [https://xmm-tools.cosmos.esa.int/external/xmm\\_user\\_support/documentation/uhb/XMM\\_UHB.pdf](https://xmm-tools.cosmos.esa.int/external/xmm_user_support/documentation/uhb/XMM_UHB.pdf) [Accessed Jan. 2017]
- [8] ESA. *About INTEGRAL*. [online] Available at: <http://www.cosmos.esa.int/web/integral/mission-overview> [Accessed Dec. 2016]
- [9] NASA. *Rossi X-Ray Timing Explorer (RXTE): December 1995 - January 2012*. [online] Available at: <https://heasarc.gsfc.nasa.gov/docs/xte/XTE.html> [Accessed Dec. 2016]
- [10] NASA. *Proportional Counter Array (PCA)*. [online] Available at: <https://heasarc.gsfc.nasa.gov/docs/xte/PCA.html> [Accessed Dec. 2016]
- [11] ESA. *IBIS: Imager on Board the INTEGRAL Satellite*. [online] Available at: <http://www.cosmos.esa.int/web/integral/instruments> [Accessed Dec. 2016]
- [12] Snowden, S., Valencic, L., Perry, B., Arida, M. and Kuntz, K. (2014). *The XMM-Newton ABC Guide: An Introduction to XMM-Newton Data Analysis*. Version 4.5. [online] Available at: [ftp://legacy.gsfc.nasa.gov/xmm/doc/xmm\\_abc\\_guide.pdf](ftp://legacy.gsfc.nasa.gov/xmm/doc/xmm_abc_guide.pdf) [Accessed Jan. 2017]

- [13] Rots, A. (1997). *JPL DE200 and DE405 in FITS; Barycenter Code* [online] Available at:  
<https://heasarc.gsfc.nasa.gov/listserv/heafits/msg00050.html> [Accessed Dec. 2016]
- [14] NASA. *gtbary - Performs barycentric or geocentric corrections to photon arrival times.* [online] Available at:  
<http://fermi.gsfc.nasa.gov/ssc/data/analysis/scitools/help/gtbary.txt> [Accessed Dec. 2016]
- [15] Kuiper, L. et al. (2009). High-energy characteristics of the schizophrenic pulsar PSRJ1846-0258 in Kes 75. *Astronomy & Astrophysics*, 501, pp. 1031-1046
- [16] Cramer, D. (1998). *Fundamental Statistics for Social Research*. First ed. London and New York: Routledge, pp. 81-82
- [17] Press, W., Teukolsky, S., Vetterling, W. and Flannery, B. (1997). *Numerical Recipes in Fortran 77: The Art of Scientific Computing*. 2nd ed. Cambridge: Cambridge University Press, pp. 604-607
- [18] Lyne, A. G., Pritchard, R. S. and Graham-Smith, F. (1993). *Jodrell Bank Crab pulsar monthly ephemeris.* [online] Available at:  
<http://www.jb.man.ac.uk/pulsar/crab.html> [Accessed Nov. 2016]
- [19] Lyne, A., Roberts, M. and Jordan, C. (2012). *Jodrell Bank Pulsar Timing Results: Monthly Ephemeris* Manchester: University of Manchester. pp. 1-3 Available at:  
<http://www.jb.man.ac.uk/pulsar/crab.html> [Accessed Jan. 2017]
- [20] Abdo, A. et al. (2010). Fermi Large Area Telescope observations of the Crab pulsar and nebula. *The Astrophysical Journal*. 708, pp. 1254-1267 (Correction in “absolute” timing value available at:  
<http://fermi.gsfc.nasa.gov/ssc/data/access/lat/ephems/> [Accessed Nov. 2016])
- [21] The VERITAS collaboration. (2011). Detection of Pulsed Gamma Rays Above 100 GeV from the Crab Pulsar. *Science*. 334, pp. 69-72, Reference 30 (See also:  
<http://fermi.gsfc.nasa.gov/ssc/data/access/lat/ephems/0534+2200/README>)
- [22] Baade, W. (1942). The Crab nebula. *Astronomical Society of the Pacific*. 54(91), pp. 188-198
- [23] NRAO, *Pulsar Properties.* [online] Available at:  
<http://www.cv.nrao.edu/course/astr534/Pulsars.html> [Accessed Nov. 2016]
- [24] ESAC, Smith, M. (2015) *XMM-Newton Calibration Technical Note, XMM-SOC-CAL-TN-0018, EPIC Status of Calibration and Data Analysis.* [online] Available at:  
<http://xmm2.esac.esa.int/docs/documents/CAL-TN-0018.pdf> [Accessed Dec. 2016]
- [25] kuiper, L. et al. (2003). Absolute timing with IBIS, SPI and JEM-X aboard INTEGRAL: Crab main-pulse arrival times in radio, X-rays and high-energy  $\gamma$ -rays. *Astronomy & Astrophysics*. 411, pp. L31-L36
- [26] Rots, A. et al. (2004). Absolute timing of the Crab pulsar with the Rossi X-ray Timing Explorer. *The Astrophysical Journal*. 605, pp. L129-L132

- [27] Molkov, S. et al. (2010). Absolute timing of the Crab pulsar with the INTEGRAL/SPI telescope. *The Astrophysical Journal*. 708, pp. 403-410
- [28] Lumb, D., Schartel, N., and Jansen, F. (2011) X-ray Multi-mirror Mission (XMM-Newton) observatory *Optical Engineering* 51(1), pp. (011009-2)
- [29] De la recherche l'industrie (CEA), *ISGRI : une camera pour l'invisible*. [online] Available at:  
[http://irfu.cea.fr/Sap/Phoce/Vie\\_des\\_labos/Ast/ast\\_visu.php?id\\_ast=1370](http://irfu.cea.fr/Sap/Phoce/Vie_des_labos/Ast/ast_visu.php?id_ast=1370) [Accessed Jan. 2017]
- [30] University of California: San Diego Center for Astrophysics and Space sciences, *RXTE*. [online] Available at:  
[http://cass.ucsd.edu/heag/RXTE\\_Photos.html](http://cass.ucsd.edu/heag/RXTE_Photos.html) [Accessed Jan. 2017]
- [31] Jodrell Bank Centre for Astrophysics *Jodrell Bank Crab Pulsar Timing Results - Monthly Ephemeris*. [online] Available at:  
<http://www.jb.man.ac.uk/pulsar/crab/crab2.txt> [Accessed Jan. 2017]